Parametric design of scaled-down pressurised thermal shock test specimens using inelastic analysis

H. E. Coules*, P. J. Orrock and C. E. Truman

Department of Mechanical Engineering, University of Bristol, Bristol, BS8 1TR, UK

*Corresponding author
Email: harry.coules@bristol.ac.uk
Telephone: +44 (0)117 331 5946

Abstract

Pressurised thermal shock tests that simulate fracture conditions relevant to nuclear reactor pressure vessels are difficult to perform and require very large specimens. This study examines the feasibility of scaled-down specimens to allow easier testing. A series of finite element models was used to design scaled-down specimens that produce a crack-driving force, crack tip temperature trajectory and constraint conditions very similar to those which occurred in a previous large-scale spinning cylinder experiment known as NESC-1. It is shown that equivalent conditions can be achieved in much smaller specimens than NESC-1 using a practical set of testing parameters.

Keywords: Thermal shock, finite element analysis, pressure vessel, spinning cylinder, J-integral

Graphical abstract

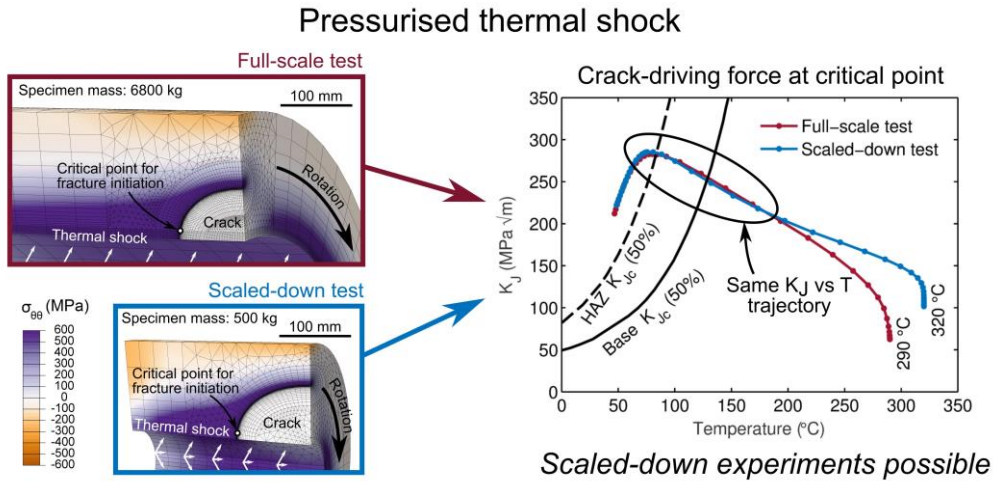

Highlights

- Thermal shock tests for nuclear reactor pressure vessels can be miniaturised.
- Models show that scaled-down tests can give equivalent fracture initiation conditions.
- Specimens equivalent to the NESC-1 thermal shock test have been designed.

1. Introduction

Pressurised Thermal Shock (PTS) is a transient condition that can occur in systems designed to retain pressure at elevated temperature. In a pressure vessel that contains crack-like flaws or defects, combinations of thermal and pressure loading may act to drive a fracture initiating from a pre-existing flaw. The possible occurrence of PTS of the Reactor Pressure Vessel (RPV) is an important consideration in the design and assessment of Pressurised Water Reactors (PWRs). Thermal shock of the RPV at high pressure, or at low pressure with subsequent re-pressurisation, could occur as a result

of unplanned events such Loss of Coolant Accidents (LOCA) and pressuriser safety valve malfunctions [1], [2]. Specifically, over-cooling of the interior of the RPV causes large tensile thermal stresses to occur close to the internal surface. This creates a risk of fracture initiation from internal surface defects. Progressive mechanisms of damage that can occur within PWRs, such as radiation-induced embrittlement of the RPV material, mean that the risk associated with thermal shock may increase over a reactor's lifetime [3].

Physical PTS tests may be used to validate analysis methods, to reveal material and structural behaviour under typical or expected conditions, and to demonstrate the validity of assessment codes [4], [5]. However, the test specimens required to simulate PWR-relevant conditions are large and so entail extremely expensive tests. Only a limited number of such tests have been performed [5], [6]. Although some previous work has been done on creating simplified methods to study PTS, this has concentrated on replicating only certain aspects of a PTS event [7], [8]. In this study, we investigate the design of scaled-down test specimens that replicate the full-scale conditions of elastic-plastic fracture during PTS. The ability to produce equivalent conditions in scaled-down specimens could greatly reduce the cost associated with qualification of RPVs and other components for which PTS is a safety consideration.

In the context of structural integrity analysis, stresses that contribute to the plastic collapse of a structure can be classed as 'primary'. By contrast, stresses that contribute to fracture but not to fully-plastic collapse are classed as 'secondary' [9], [10]. Typically, these include thermal and residual stresses which are self-equilibrating within the material. PTS is normally characterised by a combination of relatively low primary stresses due to component pressurisation and more severe secondary loading caused by the thermal transient. In many cases, pre-existing residual stresses contribute further to the secondary loading experienced by the component. The effects of primary and secondary loading on elastic-plastic fracture combine in a non-linear manner [11], [12]. The amount that secondary loading contributes to the crack-driving force depends on the nature of the fracture process; i.e. whether it occurs in a largely brittle or a largely ductile manner. Structural integrity assessment procedures including R6 Rev. 4 [10] and BS 7910:2013 [13] contain methods for determining to what extent the interaction between primary and secondary loading contributes to failure. Although such methods have developed substantially in recent years [14], they are inherently approximate.

More accurate analysis of RPVs under combined primary and secondary loading may allow their structural integrity during PTS to be demonstrated more readily. In general, the most accurate method of analysis is to use elastic-plastic Finite Element Analysis (FEA) of the cracked component, and calculate the J-integral as a function of position on the crack tip line [3]. Many examples of cracked-body FEA applied to PTS events in RPVs exist, including examples of both elastic analysis [15] and inelastic analysis [16], [17]. The elastic-plastic cracked-body FEA approach is used in the current study.

The aim of this work is to determine whether the elastic-plastic fracture initiation conditions that occur in large-scale physical PTS tests can be achieved using scaled-down test specimens. A large number of elastic-plastic cracked-body finite element analyses were performed to investigate different combinations of specimen geometry, crack geometry and test parameters with the intention of replicating the conditions present during a particular thermal shock test known as NESC-1.

2. The NESC-1 test

The PTS test that will be examined was performed by the Network for Evaluating Structural Components (NESC) in 1997 and is referred to as NESC-1 [18]. This test was chosen because it was accompanied by a substantial campaign of characterisation and modelling, and so information on the

test specimen and conditions is relatively complete. The specimen in the NESC-1 test (see Figure 1) was a hollow cylinder of ASTM A 508 Class 3 steel with a wall thickness of 175 mm, similar to the RPV of a civil PWR, and a weight of approximately 6800 kg. It was clad on the interior surface with austenitic steel, and various crack-like defects were introduced. During the test, the specimen was heated to 290°C and rotated about its axis at a nominal speed of 2100 rpm to simulate internal pressurisation of an RPV. It was then quenched with a water spray on the inner surface while still rotating. The effect of this thermal shock was monitored using strain gauges and post-test destructive analysis of the defects was performed. In addition to the experimental work, a round-robin study was carried out by NESC participating organisations to assess the accuracy of analytical and computational predictions of fracture initiation.

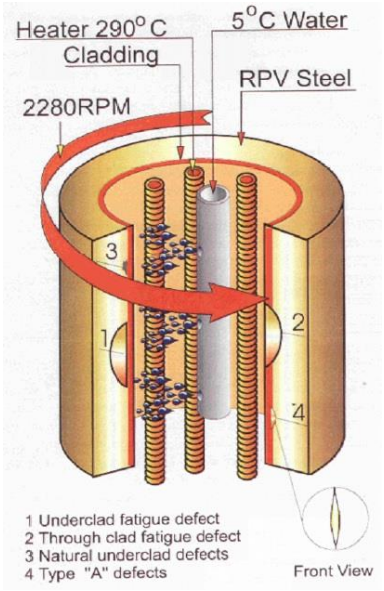

Figure 1: NESC-1 spinning cylinder test showing the specimen, various introduced defects, heating and quenching arrangements [18]*. The rotational speed indicated here is different to the initial nominal speed of 2100 rpm due to acceleration of the specimen during the test.*

The present study focusses on a single defect in the NESC-1 specimen: a crack-like through-clad semi-elliptical flaw known as Defect R. Defect R was located on the internal surface of the cylinder and was oriented in the axial-radial plane. In the NESC-1 specimen, this defect was introduced by Electrical Discharge Machining (EDM) followed by fatigue pre-cracking. The approximate dimensions of Defect R are shown in Figure 2. During the test, fracture initiation occurred in a region of the crack front close to the HAZ/base material interface, widening the defect. The fracture arrested after outward growth to a maximum extent of 16.5 mm. As illustrated in Figure 3, the fracture mechanism was initially a small amount of ductile tearing followed by cleavage fracture. Further details of the NESC-1 specimen and its materials are given by Bass et al. [18] and in Appendix 1.

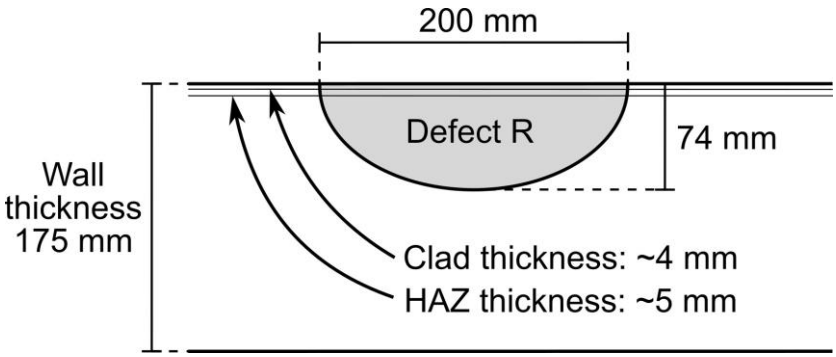

Figure 2: Nominal pre-test dimensions of Defect R. Adapted from Bass et al. [18].

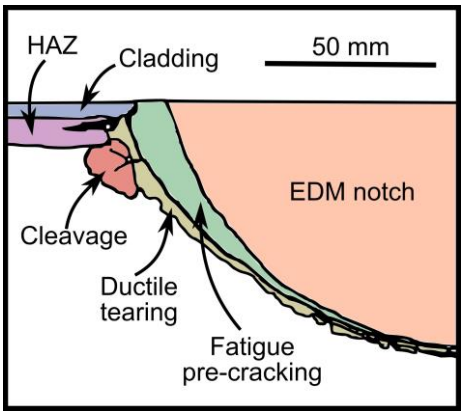

Figure 3: Detailed drawing of one side of Defect R showing the results of post-test fractographic analysis. Adapted from Rintamaa et al. [19].

The NESC-1 specimen was not designed to simulate the conditions present in a particular pressure vessel, but rather to examine the combined effect of primary and secondary loading. The centripetal loading applied during the NESC-1 test only simulates the circumferential stress that would be caused by pressurisation of an RPV (see Appendix 1). Unlike a real pressure vessel, the NESC-1 specimen wall is not loaded in the axial direction. For Defect R (which lies in the axial-radial plane) the effect of axial loading on the crack-driving force is small, although axial pressure loading would increase the level of constraint experienced at near-surface locations on the crack tip line. During the NESC-1 programme it was shown that constraint loss did not influence fracture initiation at this defect in the spinning-cylinder specimen [18]. Therefore in terms of fracture initiation at Defect R, the NESC-1 specimen behaved similarly to an equivalent pressure vessel and the differences in constraint inherent to the spinning-cylinder test design were not significant in this case. However, in general it is important to consider the differences in crack tip constraint with respect to a real pressure vessel when designing this type of test.

3. Modelling

3.1 Overview

The NESC-1 test was simulated using cracked-body thermal-elastic-plastic FEA. A parametric series of simulations of different scaled-down tests was then performed to determine what test conditions could produce equivalent crack front loading conditions to those encountered at full-scale. The crack loading conditions that occurred at two locations on the crack tip line in Defect R were examined in detail. The locations of interest were the deepest point on the crack and the point where fracture was observed to initiate in the NESC-1 test, which represented the most severe loading condition on the

crack tip line. The location of fracture initiation was roughly at the interface between the base material and the Heat Affected Zone (HAZ) of the cladding, 14 mm from the inner surface of the specimen. Preliminary linear-elastic models were also performed to ensure that they agreed with weight function analysis (see Appendix 2).

The thermo-elastic-plastic simulations of NESC-1 and the scaled-down tests required both heat transfer analysis and mechanical analysis. They used an uncoupled analysis in which the thermal field was assumed to be independent of any mechanical effects. Heat transfer analysis was performed first, and then the resulting time-dependent thermal field was imposed during modelling of the specimen's mechanical deformation. All of the FEA was performed using the Abaqus/Standard v6.12 solver [20], with model generation and meshing done using Abaqus/CAE v6.12 [21]. For analysis of the scaled-down specimens, automatic model generation and execution for a large series of parametric models was carried out using purpose-built MATLAB code [22] in conjunction with the Abaqus/CAE Python scripting interface. This is described in Appendix 3.

3.2 Thermo-elastic-plastic modelling of the NESC-1 PTS test

Thermo-elastic-plastic modelling of the NESC-1 PTS test was performed to provide the baseline against which analyses of scaled-specimen tests (described in Section 3.3) could be compared and also to investigate two modelling simplifications which would be important for the later parametric study. To simplify the model, the effect of including or excluding the differences in mechanical properties of the HAZ and clad layers with respect to the base material was examined, as was the effect of including or excluding the cladding residual stress.

A thermal finite element model was developed to determine the unsteady temperature field in the NESC-1 cylinder during quenching. Although the heat transfer in the specimen was essentially 1-dimensional, a 3-dimensional thermal model was used so that the thermal result could be easily transferred onto the subsequent mechanical model. The thermal model used 8-noded linear brick elements throughout and the presence of Defect R was not modelled. The defect was assumed to have no effect on heat transfer because the direction of heat flow was essentially radial and the defect lay in the axial-radial plane. The differing thermal conductivity of the clad material with respect to the base material was shown to affect the heat transfer significantly during the NESC-1 test [23]. Therefore, in all of the thermal models used in this study two separate regions of the mesh were defined: one representing the cladding material and one representing the HAZ and base material. Different thermal conductivity properties were used in each region (see Appendix 1).

A surface film heat transfer condition was applied to simulate water-quenching of the internal surface of the cylinder. A sink temperature of 5°C was used (the temperature of the cooling water) and a surface film coefficient of 9 kW m^{-2} K^{-1} was adopted (see Appendix 4). It was assumed that heat transfer from the external surfaces of the specimen, which were insulated during the NESC-1 test, was negligible.

The mechanical model used a different mesh to the thermal model, accounting for the presence of Defect R. Defect R was modelled as a perfectly-sharp crack-like semi-elliptical defect with a depth of 74 mm and a surface length of 200 mm, which was a very good approximation to its measured initial dimensions (see Figure 2). Additional partitioning of the cylinder, shown in Figure 4, was performed so that appropriate material properties and mesh refinement could be applied for the clad and HAZ. The clad was modelled as having a uniform thickness of 4 mm, with a uniform 10 mm HAZ beneath. All assumptions regarding the cladding and defect geometry were the same as those used in modelling work carried out during the NESC-1 programme. This mesh had regions of 8-noded linear brick elements around the crack tip, in the clad and HAZ, and remote from the crack. 6-noded full-

integration linear wedge elements were used at the crack tip. 10-noded quadratic tetrahedral elements were used in an unevenly-shaped region enclosing the crack. This meshing arrangement was designed for computational efficiency and for adaptability to different geometric parameters, both of which were important for the parametric study described in Section 3.3. Preliminary studies showed that this meshing arrangement produced results of similar accuracy to more complex meshes incorporating collapsed quadratic elements at the crack tip. Rotation of the specimen about its axis was simulated by applying a non-uniform body force. Quenching was simulated by imposing the unsteady temperature field calculated using the thermal model. The specimen materials were modelled using temperature-dependent elastic properties, plastic properties and coefficients of thermal expansion (see Appendix 1). The materials were assumed to obey isotropic rate-independent strain-hardening behaviour, and cyclic hardening effects were not considered.

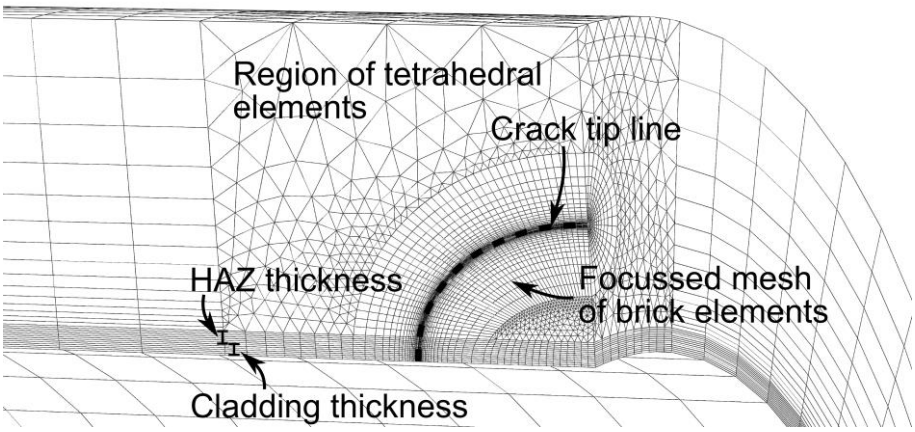

Figure 4: Finite element mesh surrounding the defect in a model used for EPFM analysis of Defect R in the NESC-1 specimen.

The elastic-plastic crack driving force at any given point on Defect R was estimated using the J contour integral [24], [25]:

$$J = \int_{\Gamma} \left(w\delta_{1j} - \sigma_{ij}u_{i,1}\right)n_j \, ds + \int_{A} \sigma_{mn}\alpha_{mn}T_{,1} \, dA \qquad (1)$$

where w is the strain energy density, σ_{ij} is the stress tensor, u_i is the displacement vector, δ_{ij} is the Kronecker delta, s is the distance along a contour Γ surrounding the crack tip for which n_j is an outward-facing normal vector, α_{mn} is the material's thermal expansion tensor, T is the temperature and A is the area enclosed by Γ. The J-integral was calculated from the modelled stress and displacement fields using the equivalent domain integral method [26].

The mechanical model of the NESC-1 was run three times using different assumptions regarding the clad/HAZ region:

1. The differences in the mechanical properties of the clad and HAZ material with respect to the base material were included in the model, and so was the initial residual stress which resulted from cladding (see Appendix 1).
2. The different clad and HAZ mechanical properties were included in the model, but the residual stress was not.
3. The clad and HAZ were modelled using the same mechanical properties as the base material and residual stress was not included.

By comparing the results of these three models it was found that neither the clad mechanical properties nor the residual stress significantly affected the elastic-plastic crack-driving force at locations of interest on the crack front (i.e. at the HAZ/base interface and at the deepest point on the crack). Therefore, all models used in the parametric study described in Section 3.3 did not include these factors.

3.3 Parametric study for the design of scaled-down specimens

A parametric study was performed to identify scaled-down specimen geometries that could be used to create elastic-plastic crack front loading conditions equivalent to those in the NESC-1 test. Models were performed using every combination of the parameters listed in the right-hand column of Table 1, i.e. a total of 324 models. The geometric parameters $\frac{R_i}{R_o}$, R_o and $\frac{a}{t}$ (see Figure 5) were varied, while the crack aspect ratio $\frac{a}{c}$ was the same for all models. The rotational speed ω and initial temperature T_0 were also varied. The parameter ranges were selected on the basis of practicality: the range of cylinder outer radius was chosen to give specimens compact enough for easy manufacture and handling, while being large enough to produce the required crack-driving force under reasonable rotation and quenching conditions. Angular velocities above 10,500 rpm were considered impractical. Initial temperatures above 400°C were not considered due to a lack of material data in this range, and the possibility of thermally-induced microstructural change. Model generation and execution was automated using purpose-built programs written in MATLAB [22], as described in Appendix 3.

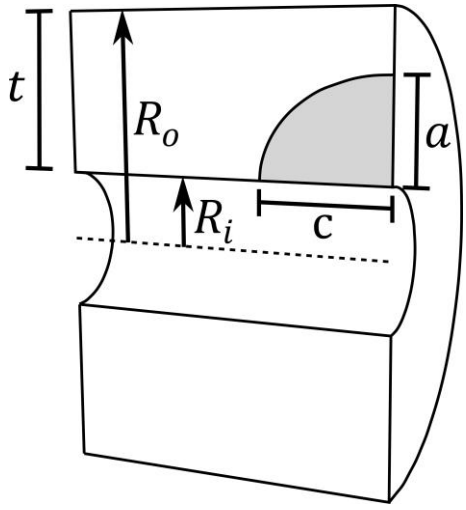

Figure 5: Geometric features of a scaled-down cylinder specimen (quarter specimen shown).

Parameter	Symbol	NESC-1 value	Main parameter set
Cylinder radius ratio	$\frac{R_i}{R_o}$	0.7491	0.3, 0.5, 0.7491
Cylinder outer radius	R_o	697.5 mm	150, 200, 250 mm
Normalised crack depth	$\frac{a}{t}$	0.4229	0.4229, 0.6, 0.7
Crack aspect ratio	$\frac{a}{c}$	0.74	0.74
Rotational speed	ω	2100 rpm	2100, 6300, 8400, 10500 rpm
Initial temperature	T_0	290°C	290, 350, 400°C

Table 1: Range of parameters used in the parametric study.

For each set of parameters a thermal model was run followed by two cracked-body mechanical models using purely-elastic mechanical properties and elastic-plastic properties respectively. The elastic-plastic model was used to calculate the J-integral, while the purely elastic model was used to calculate the elastic T-stress in order to estimate the level of crack tip constraint. All of the mechanical models used in the parametric study (Figure 6) assumed that the cladding and HAZ had mechanical properties identical to the base metal and contained no initial residual stress.

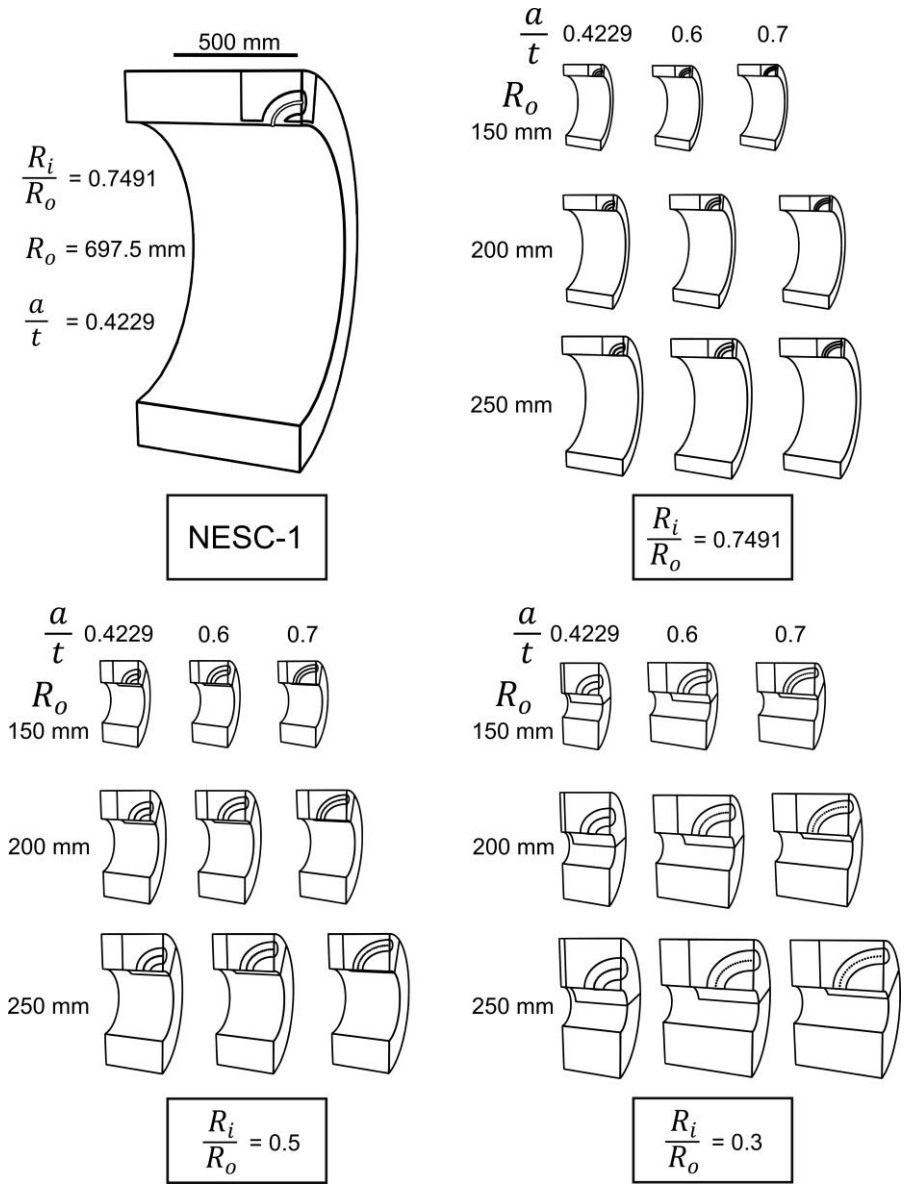

Figure 6: Specimen geometries used in the parametric study shown to scale alongside the NESC-1 specimen. For each of the specimen geometries shown above, 12 models were run with different angular velocities ω and initial temperatures T_0 given in Table 1.

4. Results

4.1 Modelling of NESC-1 Defect R

Three different models of the NESC-1 test were performed using different assumptions regarding the clad and HAZ (see Section 3.2). The elastic-plastic crack driving force during quenching at different points on the crack tip line for each of the three models is shown in Figure 7. The crack driving force is presented using the elastic-plastic equivalent stress intensity factor K_J which is calculated from the J-integral using:

$$K_J = \sqrt{J \frac{E}{1 - \nu^2}} \tag{2}$$

where E is the Young's modulus of the material and ν is its Poisson's ratio (see Table 2). Although the presence of residual stress and differing mechanical properties affects the crack-driving force at points on the crack tip line within the cladding, and to an extent those in the HAZ, these factors have little effect at the HAZ/base interface and in the base material. Therefore, these factors were omitted from the subsequent parametric study described in Section 3.3.

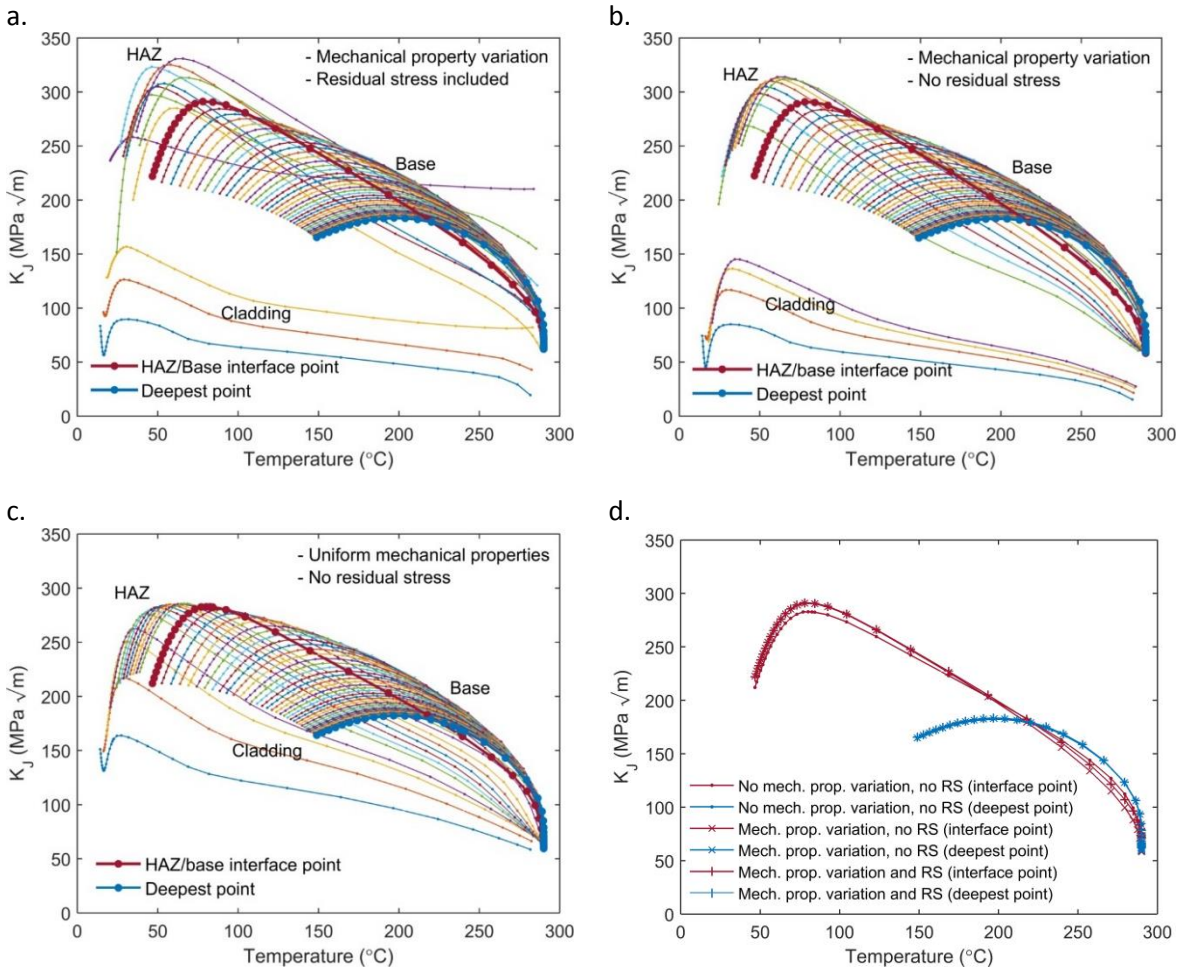

Figure 7: Elastic-plastic equivalent stress intensity factor as a function of crack tip temperature for Defect R during the NESC-1 quench. Each coloured line shows the K_J vs temperature trajectory for a different point on the crack. Captions indicate the general regions of the crack tip line: locations within the cladding, HAZ and base material. a-c.) Show three models with different levels of modelling fidelity for the clad. Labels indicate which points occur in the cladding, HAZ and base material. d.) Direct comparison for the deepest point and the HAZ/base interface point only.

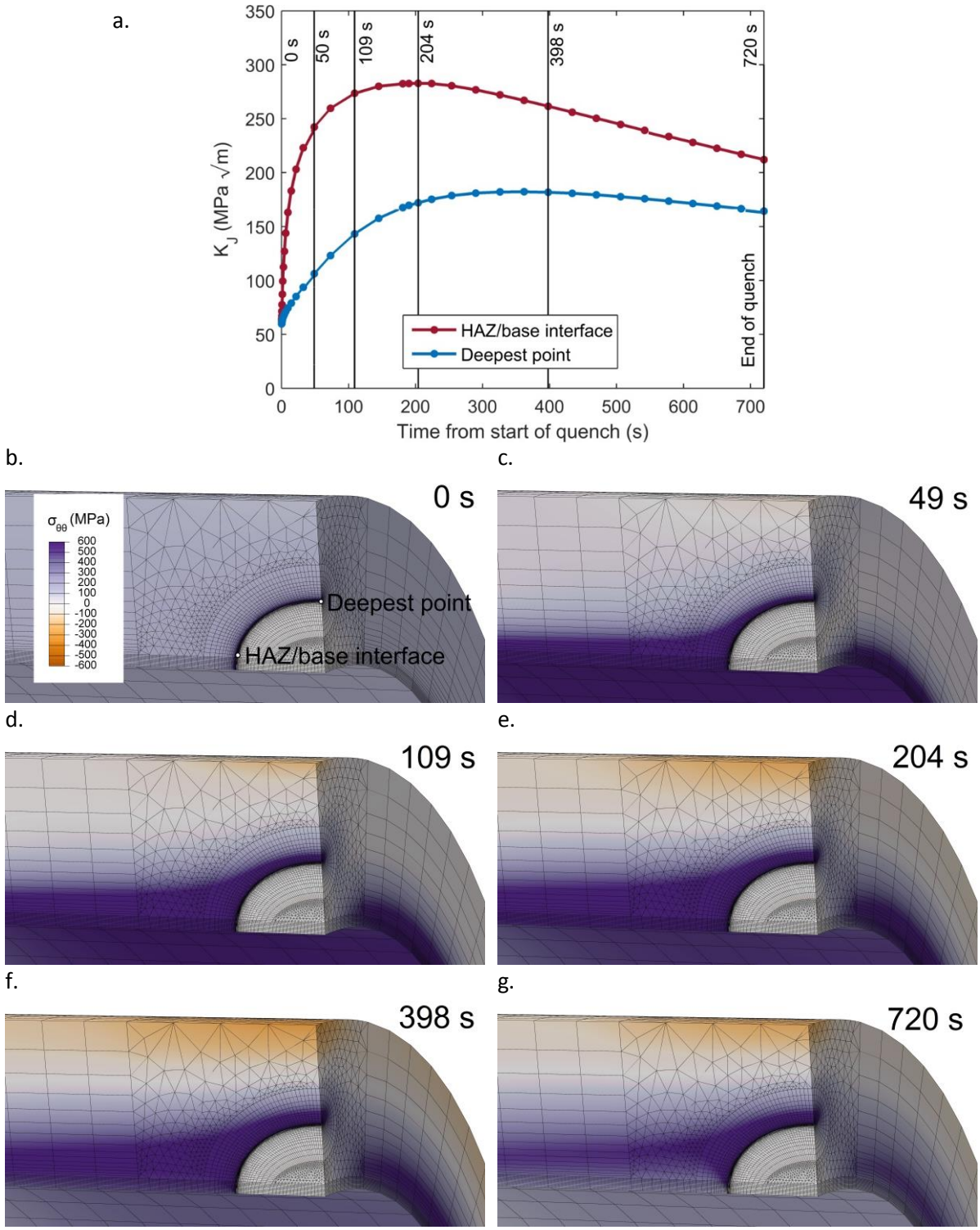

Figure 8: Crack-driving force and stress field history during quenching of the NESC-1 specimen. a.) Elastic-plastic equivalent stress intensity factor. b-g.) Stress field at Defect R (circumferential component shown). As in Figure 7c, this model does not consider residual stress or the differing mechanical properties of the clad.

The stress field surrounding Defect R during quenching is shown in Figure 8 for a model with no residual stresses or mechanical property variation. At the start of the quench (Figure 8b) the stress field is tensile in the circumferential direction due to rotation of the specimen. Remote from the crack this circumferential stress ranges from +117 MPa on the outer surface to +183 MPa on the inner surface, which is in agreement with the results of elastic analysis shown in Figure 16. Quenching causes contraction of the material close to the cylinder's inner surface which leads to increased tensile stress

here and hence further loading of the crack tip line (Figure 8c-e). As the quench progresses and the through-wall temperature gradient drops, the stress field close to the inner surface is partially relaxed causing significant unloading of the crack close to the inner surface (Figure 8f-g). The effect of this cycle on the elastic-plastic crack driving force is shown in Figure 8a and the final distribution of plastic strain is shown in Figure 9.

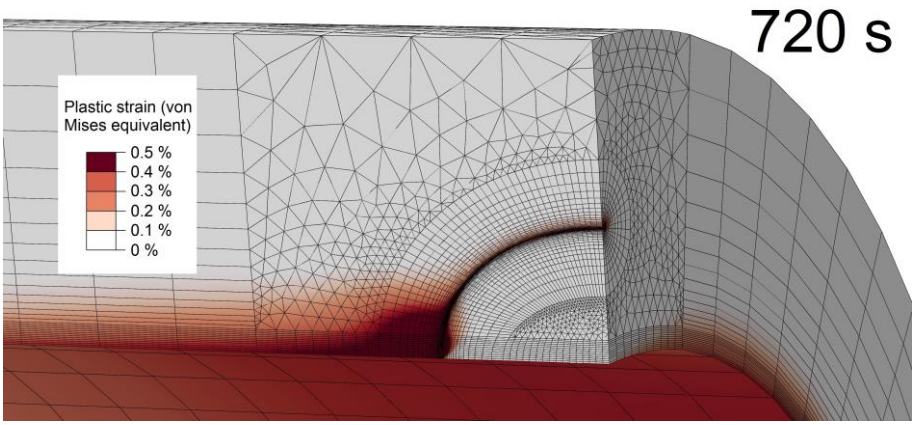

Figure 9: Plastic strain around Defect R after quenching, from a model incorporating no residual stress or mechanical property variation.

The J -integral is only strictly independent of the contour over which it is evaluated under proportional loading conditions, which may be approximated during monotonic loading of a non-linear elastic material [27]. However, in all of the models in this study incremental flow plasticity is used. Furthermore, during this thermal shock event the unsteady thermal field causes partial unloading of some regions of the crack tip line towards the end of the thermal cycle, which violates the condition of monotonic loading. Towards the end of the quenching thermal cycle some path-dependence of the contour integral results was observed at crack tip points close to the inner surface of the specimen, including the HAZ/base interface point shown in Figure 10b. However, the observed path-dependence was slight and the J-integral reached stabilised values at a small distance from the crack tip in all cases. Since the purpose of the models was to investigate the most severe loading condition at any point rather than the less severe (i.e. partially-unloaded) conditions which occurred later in the thermal cycle, and since loading-up to the most severe condition during quenching was largely monotonic, path-dependence of the J-integral did not affect the results significantly.

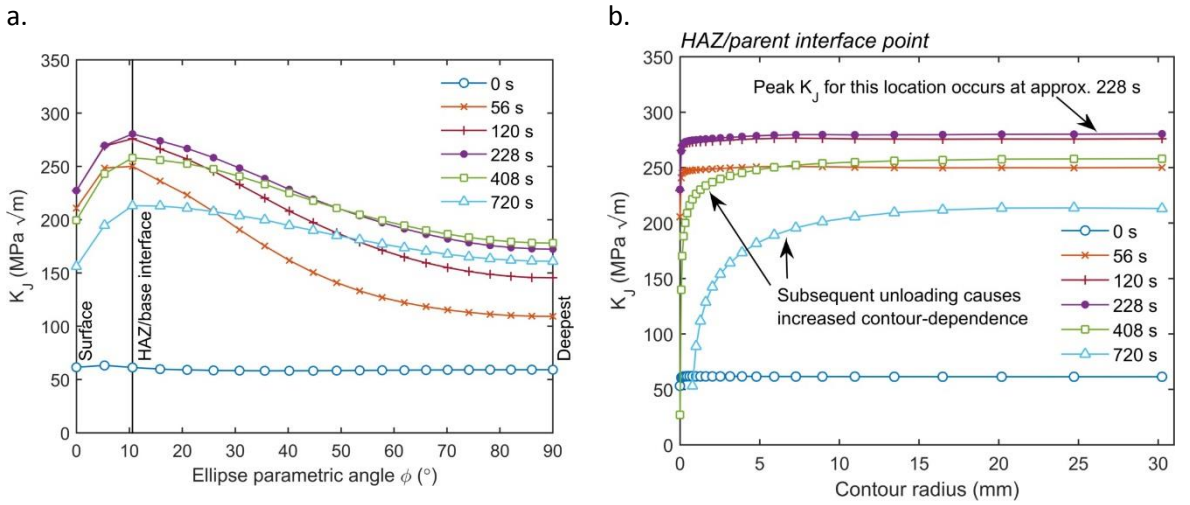

Figure 10: Variation in elastic-plastic equivalent stress intensity factor a.) over the NESC-1 Defect R crack tip line, b.) as a function of contour radius for the HAZ/parent interface point.

The results from thermo-elastic-plastic cracked-body modelling of Defect R are compared with the results of models performed during the NESC-1 programme in Figure 11. There is good agreement in terms of elastic-plastic crack driving force both at the HAZ/base material interface and at the deepest point in the crack. In Figure 11a the crack-driving force line crosses the lines indicating the temperature-dependent plane strain fracture initiation toughness of the HAZ and base materials, indicating that fracture initiation will occur at this location – as indeed it did in the real NESC-1 specimen (see Figure 3). By comparing the K_J vs temperature lines for all points on the crack tip line (Figure 7) with the material fracture toughness lines shown in Figure 11a, it was confirmed that fracture should first initiate at the HAZ/base interface.

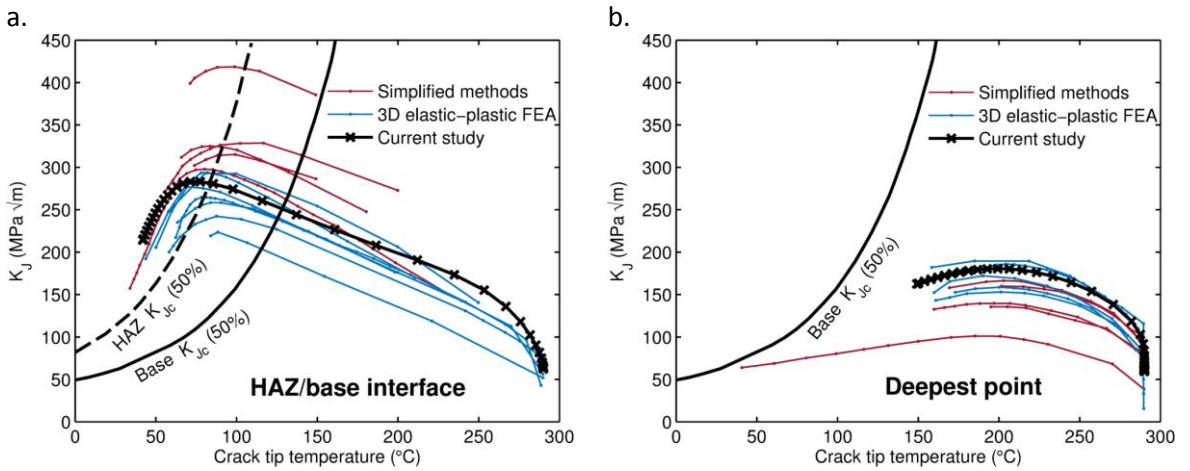

Figure 11: Elastic-plastic equivalent stress intensity factor for two points on Defect R, as calculated in this study and by different participants in the NESC-1 progamme modelling round-robin [18], [28]. *Line colour indicates the analysis method used by each NESC-1 participant. a.) HAZ/base interface 14 mm from the specimen's innner surface. b.) Deepest point in the crack.*

4.2 Scaling of PTS fracture initiation tests

To achieve equivalence in fracture initiation conditions, it is necessary to produce the same peak crack-driving force and constraint conditions in a scaled-down specimen as occurs at the site of fracture initiation in a full-scale test. In addition, the fracture properties of the materials used in the NESC-1 specimen were strongly temperature-dependent. Therefore, it is important for this peak crack-driving force to occur at the same temperature in the scaled-down specimen. The parametric

models described in Section 3.3 produced a large number of results which were examined to identify combinations of test parameters that gave equivalent fracture initiation conditions to NESC-1.

Within the range of parameters for which models were performed (Table 1) there were several sets of conditions under which the same peak crack-driving force was achieved at the same temperature as in NESC-1 Defect R. Figure 12 shows an example: the contour plots are from three scaled tests which had identical parameters except for the temperature prior to quenching, T_0. Figure 12a shows K_J vs crack tip temperature for NESC-1 and for the scaled-down tests. The parametric study indicates that the required combination of peak K_J and crack tip temperature could be achieved in a scaled-down test with an initial temperature of 320°C, and this was confirmed using an additional analysis. The K_J vs temperature trajectory for the critical location in this scaled-down test is almost identical to NESC-1 over the range of K_J where fracture may initiate.

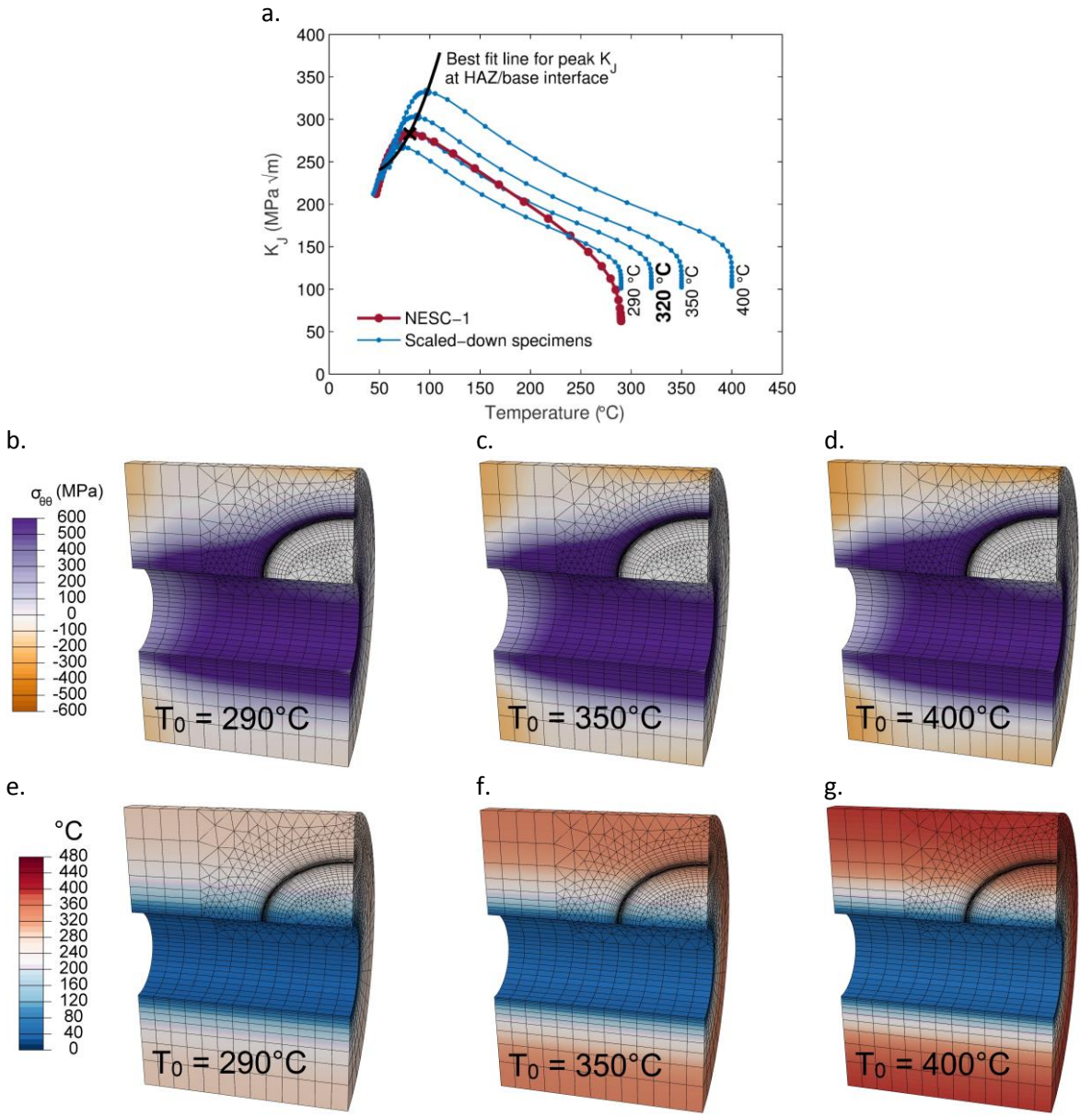

Figure 12: a.) K_J vs crack tip temperature for the HAZ/base interface point in NESC-1 Defect R and in three scaled-down tests. b.-g.) Stress and temperature distributions at the instant of peak K_J. The scaled-down test parameters are: $\frac{R_i}{R_o} = 0.3$, $R_o = 200\ mm$, $\frac{a}{t} = 0.6$, $\frac{a}{c} = 0.74$, $\omega = 10{,}500\ rpm$, $T_0 = 290, 350, 400$℃.

In addition to the peak crack driving force and the temperature at which this occurs, the level of crack tip constraint was also considered. This was done by calculating the elastic T-stress which occurred during quenching in perfectly elastic cylinders with the same dimensions and quench parameters as those used to calculate J and K_J. Although T-stress characterisation of crack tip constraint is only rigorously applicable to linear-elastic materials, it has been shown that the elastic T-stress can also be used to indicate constraint loss at cracks in elastic-plastic materials [29], [30]. Figure 13 shows the elastic T-stress along the crack tip at several instants during the quenching thermal cycle for the NESC-1 specimen and for one of the scaled-down specimens shown in Figure 12a. In the NESC-1 specimen (Figure 13a), the T-stress at the HAZ/base interface point remains positive throughout the quench, indicating that there is no loss of constraint here. For the scaled-down specimen (Figure 13b) there is some constraint loss at the HAZ/base interface, but only towards the end of the thermal cycle. During the occurrence of a peak in elastic-plastic crack driving force at the HAZ/base interface there is no constraint loss at this point.

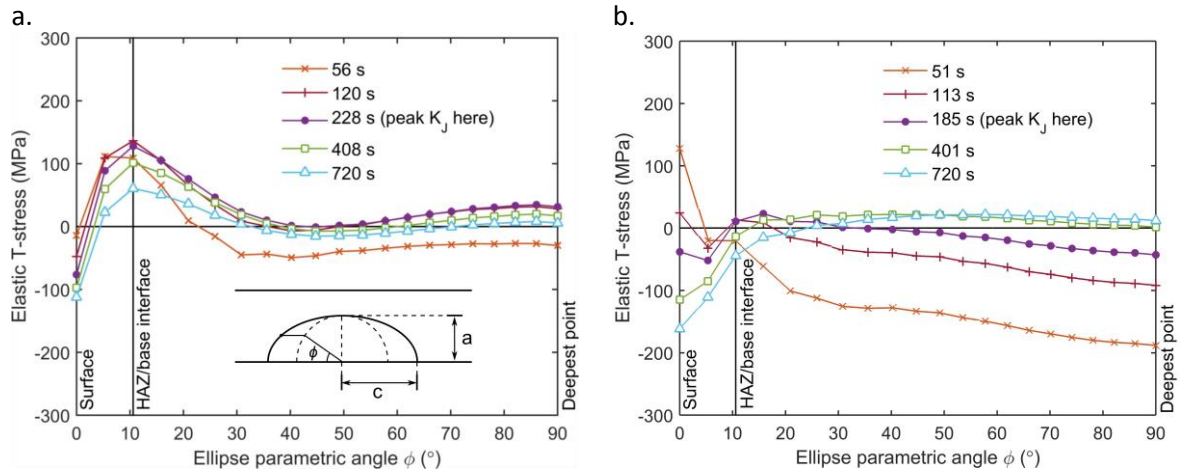

Figure 13: Elastic T-stress as a function of position on the crack tip in: a.) NESC-1 specimen, b.) scaled-down specimen as shown in Figure 12a with $T_0 = 320$°C.

5. Discussion

5.1 Modelling of PTS

In this study, thermo-elastic-plastic cracked-body FEA was used to study the conditions for fracture initiation at a crack subjected to combined primary and secondary loading. The conditions analysed are representative of a very severe pressurised thermal shock. The elastic-plastic fracture parameter results shown in Figure 11 demonstrate good agreement with previous analyses of NESC-1 and correctly predict the location of fracture initiation that was observed experimentally. The occurrence of the critical location for fracture initiation during PTS at the HAZ/base interface has recently been reported for a similar case by Chen et al. [31].

In the NESC-1 specimen the residual stress in the clad, and the differing mechanical properties of clad material with respect to the base material, have no significant influence on crack initiation at Defect R. Although these factors do affect the development of stress and crack-driving force in the clad (see Figure 7), the clad has a low yield strength relative to the base material and is not a critical location for fracture initiation.

5.2 Feasibility of scaled-specimen PTS experiments

A parametric study has shown that the peak elastic-plastic crack driving force that occurred during the NESC-1 PTS test could be achieved at the same crack tip temperature in a scaled-down quenched spinning-cylinder specimen. Several sets of parameters where similar conditions could be achieved have been identified, and an example is shown in Figure 12. The scaled-down specimen shown in this example would weigh approximately 500 kg in comparison to NESC-1's 6800 kg. With further optimisation of the geometry and loading it may be possible to design even smaller specimens that would produce very high elastic-plastic crack loading for their size under PTS conditions. This is significant given the difficulty and cost involved in performing large-scale thermal shock tests: any reduction in the specimen size could have considerable practical benefits. More generally this study demonstrates that through the use of elastic-plastic cracked-body FEA, scaled-down specimens can be designed to produce equivalent conditions for fracture initiation even under complex loading modes. The thermal shock event imposed on the NESC-1 specimen was substantially more severe than postulated LOCA transients for a PWR [18], which makes it an excellent test of the feasibility of scaled-specimen experiments. If the most severe conditions present on NESC-1 Defect R can be replicated in a smaller specimen, then it is very likely that the same method could also be used to study cases where less severe loading is required.

Fracture initiation under PTS conditions does not depend solely on J and the crack tip temperature; it may also be affected by the level of crack tip constraint [15]. The elastic T-stress calculated under linear-elastic conditions provides a qualitative indication of constraint loss [29], [30]. The T-stress results shown in Figure 13 indicate that although the scaled-down specimen developed a different crack-line distribution of T-stress in comparison to the full-scale specimen, there was no loss of constraint at the critical location for fracture initiation. The fracture initiation behaviour in this particular scaled-down specimen is therefore unlikely to be different with respect to a full-scale specimen as a result of constraint loss. However, the same might not be true for any scaled-down PTS test. So, as with other fracture mechanics specimens, it is important to consider constraint in the design of scaled-down PTS specimens. Cracked-body FEA provides a means to predict the constraint conditions which occur during PTS and hence ensure equivalence between full-scale and scaled-down tests.

The effects of specimen scaling on crack growth and arrest were not investigated here; only the effect on fracture initiation. Differing combinations of primary and secondary stress may have different effects during crack extension [32], [33]. To simulate the processes of crack growth and arrest, it would be necessary to ensure that similar crack-driving force conditions occurred in the scaled-down test not just at the initial crack length but also at a range of crack extensions. This would be more difficult than considering fracture initiation alone. However, for small amounts of crack extension it would be possible to produce conditions that were similar to those in a larger PTS test, to a useful degree of accuracy. This could be done through careful experimental control of the ratio of primary loading (in this case caused by specimen rotation) to secondary loading (caused by thermal shock).

6. Conclusions

1. The fracture initiation conditions that occur in nuclear pressure boundary components during PTS events could be produced using scaled-down test specimens made of identical materials. Scaled-down specimen parameters that would give equivalent conditions to the NESC-1 test have been identified.
2. The design of a scaled-down PTS specimen and test procedure requires accurate prediction of the crack tip conditions. Without 3D cracked-body FEA it would be difficult to ensure that the conditions which existed in the scaled-down specimen were equivalent to those in a real component.
3. Since the level of crack tip constraint may be different in a scaled-down specimen with respect to a full-scale one, this factor should be considered carefully during the design of any scaled PTS test.
4. For NESC-1 Defect R, the residual stress in the clad and the difference in mechanical properties of the clad with respect to the base material had no significant influence on fracture initiation, although the effect of the clad's differing thermal conductivity was significant.
5. Crack propagation and arrest were not investigated in this study but the results suggest that for short crack growth during PTS, equivalent conditions could be achieved in a scaled-down specimen to a reasonable degree of accuracy.

7. Acknowledgements

This study was funded by Frazer-Nash Consultancy Ltd. and the UK Ministry of Defence under the Sustaining Independent Nuclear Expertise (SINE) programme. The authors are grateful to Brian Gribben, Mike Anderson and Jonathan Douglas of Frazer-Nash Consultancy for managing and reviewing this work.

8. Supplementary data

Results from the models described in this article are available as supplementary data. They can be downloaded from: [INSERT DOI LINK HERE]

Appendix 1: NESC-1 material and residual stress characterisation

The NESC-1 study included a comprehensive programme of material and defect characterisation. A summary of the basic properties of the NESC-1 cylinder materials is given in Table 2.

Property	Considered temperature-dependent	Value at 20°C		
		Base	HAZ	Clad
Density	Yes	7800 kg m^{-3}	7800 kg m^{-3}	7720 kg m^{-3}
Thermal conductivity	Yes	40.41 W m^{-2} K^{-1}	40.41 W m^{-2} K^{-1}	14.26 W m^{-2} K^{-1}
Specific heat capacity	Yes	440.2 J kg^{-1} K^{-1}	440.2 J kg^{-1} K^{-1}	440.2 J kg^{-1} K^{-1}
Coefficient of thermal expansion	Yes	11.88 10^{-6} K^{-1}	11.88 10^{-6} K^{-1}	15.89 10^{-6} K^{-1}
Young's modulus	Yes	210.5 GPa	210.5 GPa	148.5 GPa
Poisson's ratio	No	0.28	0.28	0.28

Table 2: Summary of the properties of the NESC-1 specimen materials at ambient temperature. The models in the current study used temperature-dependent material properties.

During NESC-1, tensile tests of the base, HAZ and clad materials were performed at ambient temperature and at elevated temperatures [5]. The results are shown in Figure 14. The stress-strain curve of the austenitic cladding material was strongly dependent on the test temperature, and so temperature-dependent flow curves were used for this material. By contrast, the ferritic base material and the HAZ exhibited plastic properties which were not strongly dependent on temperature within the temperature range encountered during the PTS test (5 – 290°C). Therefore, in the present work the plastic flow curves of the base and HAZ materials were taken to be invariant with temperature for modelling purposes. All of the materials were assumed to exhibit isotropic hardening behaviour and cyclic hardening was not considered. The Young's modulus, thermal conductivity, specific heat capacity and coefficient of thermal expansion of the specimen materials were assumed to be linear functions of temperature, as was the case during the NESC-1 programme [18].

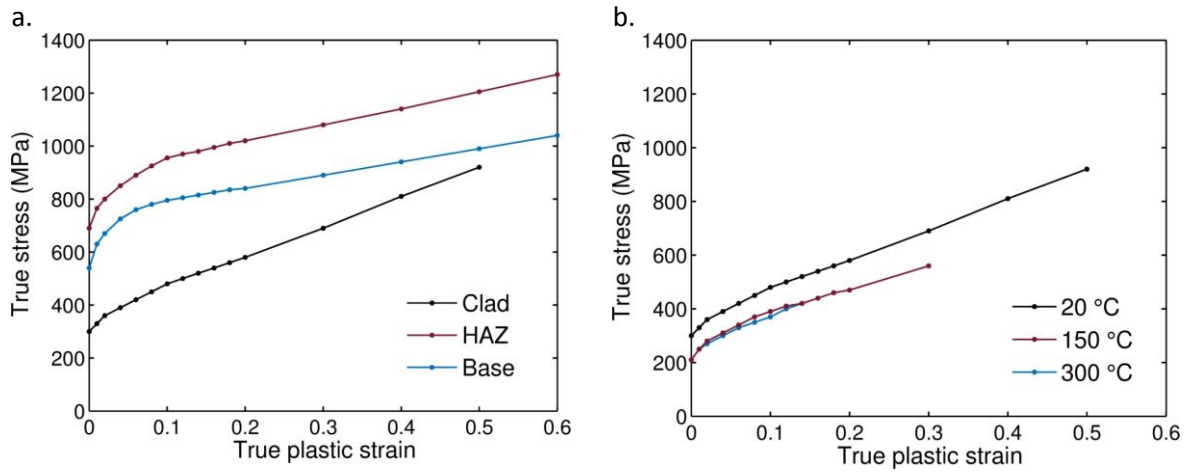

Figure 14: Plastic properties of the specimen materials. a.) Base, HAZ and clad material at 20°C. b.) Clad material at elevated temperatures [18].

After the internal cladding was applied to the NESC-1 cylinder, it was subjected to Post-Weld Heat Treatment (PWHT) at 550°C. Significant residual stresses remained in the clad after heat treatment and this was partly attributed to the difference in thermal expansion between the base and cladding

materials (see Table 2). The residual stress in the clad prior to the PTS test was measured using the ring core method [18], [34]. The through-thickness residual stress distribution is shown in Figure 15 for the circumferential stress direction ($\sigma_{\theta\theta}$). In this work, it is assumed that the initial residual stress in the clad and the material beneath it had this through-thickness distribution. Although the data in Figure 15 is for the $\sigma_{\theta\theta}$ direction only, in the absence of data for the other components of the stress tensor it was assumed that the stress state was approximately equi-biaxial, as is typical in a clad layer. In models which included the effect of residual stress, the residual stress field was imposed as an initial condition by using the Abaqus/Standard keyword *INITIAL CONDITIONS, TYPE=STRESS and defining the stress components explicitly for each model element. After the residual stress was imposed, an extra step was included in the model to establish a self-equilibrating residual stress field before the start of the main PTS simulation.

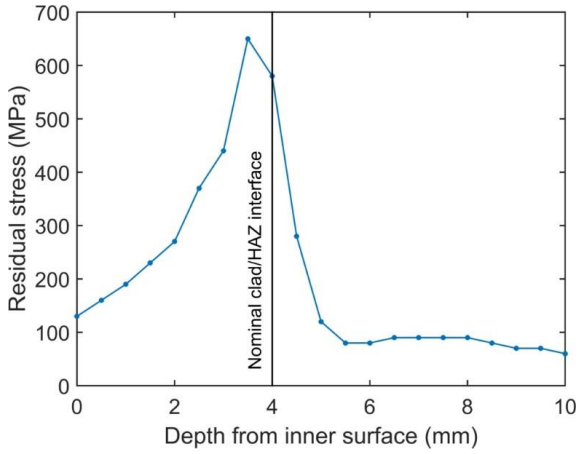

Figure 15: Measured through-thickness distribution of circumferential residual stress in the clad [18].

Appendix 2: Elastic modelling of the NESC-1 specimen

Prior to full thermo-elastic-plastic modelling of the NESC-1 PTS test, linear elastic analysis of Defect R under centripetal loading alone was used to confirm the accuracy of the cracked-body modelling approach. Stress intensity factors calculated via FEA of the cracked specimen were compared with the results of weight function analysis using the stress distribution for an equivalent un-cracked elastic cylinder. For the cracked body analysis, the same model geometry and mesh as described in Section 3.2 were used. The specimen material was considered to be perfectly elastic and free of residual stress, and the cylinder was subjected to simple rotation without thermal shock. The resulting Mode I stress intensity factor as a function of position on the crack tip was calculated using the contour integral method.

First, the distributions of stress through the thickness of the rotating cylinder were compared. The distributions of radial and circumferential stress in an elastic hollow cylinder rotating about its axis are [35]:

$$\sigma_{rr} = \left(3 + \frac{\nu}{1-\nu}\right)\frac{\rho\omega^2}{8}\left[R_i^2 + R_o^2 - \frac{R_i^2 R_o^2}{r^2} - r^2\right] \quad (3a)$$

$$\sigma_{\theta\theta} = \frac{\rho\omega^2}{8}\left[\left(3 + \frac{\nu}{1-\nu}\right)\left(R_i^2 + R_o^2 + \frac{R_i^2 R_o^2}{r^2}\right) - \left(1 + \frac{3\nu}{1-\nu}\right)r^2\right] \quad (3b)$$

where σ_{rr} and $\sigma_{\theta\theta}$ are the radial and circumferential stress components respectively, R_i and R_o are the cylinder's inner and outer radii respectively, ν is the Poisson's ratio of the material, ρ is its mass

density, ω is the rotational speed and r is the radial dimension. This stress distribution is plotted in Figure 16 alongside the results of the cracked-body analysis (for a region remote from the crack) and an uncracked-body analysis. There is very good agreement between the three analyses.

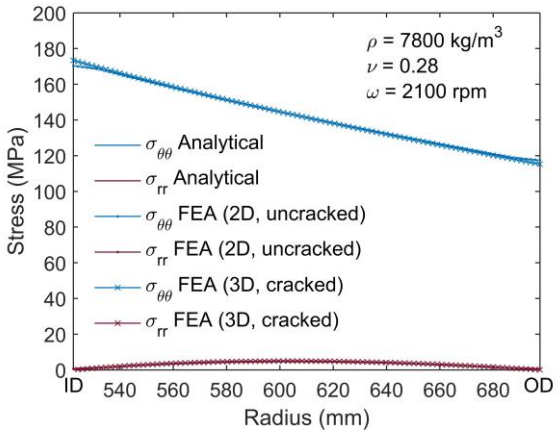

Figure 16: Stress distributions through the wall of an elastic spinning cylinder calculated via three methods. The result for cracked-body FEA is shown for a region remote from the crack.

Mode I SIFs for the deepest point on Defect R and its intersections with the cylinder interior surface were calculated from the analytical solution given in Equation 3 using weight function coefficients provided by Chapuliot [36]:

$$K_I = \sqrt{\pi a}\left[\sigma_0 i_0 + \sigma_1 i_1 \frac{a}{t} + \sigma_2 i_2 \left(\frac{a}{t}\right)^2 + \sigma_3 i_3 \left(\frac{a}{t}\right)^3\right] \quad (4)$$

where K_I is the Mode I SIF, $\sigma_{0\ldots3}$ are the coefficients of a third-degree polynomial representing the through-wall distribution of circumferential stress, $i_{0\ldots3}$ are weight function coefficients which depend on the cylinder and crack geometry, a is the crack depth and t is the cylinder wall thickness. The weight function coefficients given by Chapuliot were interpolated linearly so that they could be used with the NESC-1 cylinder and defect geometry. This method predicted stress intensity factors for NESC-1 Defect R at 2100 rpm of 58.15 MPa √m at the deepest point and 60.92 MPa √m at the surface points. Figure 17 shows that this is in agreement with the results of the elastic cracked-body analysis.

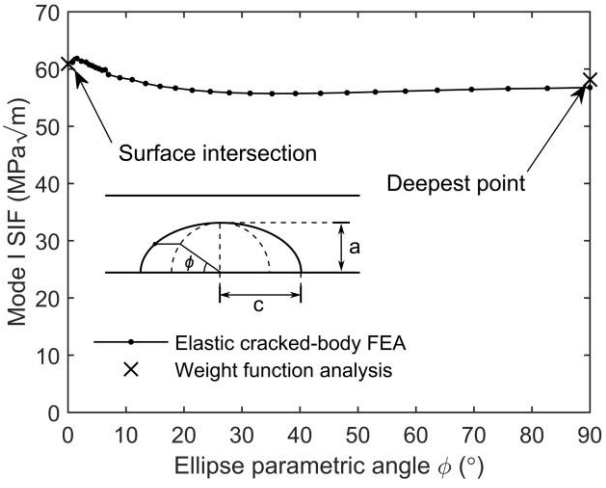

Figure 17: Comparison of stress intensity factor for Defect R at 2100 rpm calculated using cracked-body FEA and weight function analysis. Inset shows crack geometry (not to scale).

Appendix 3: Parametric series of PTS models

To deal with variation in geometry of the cylinder and defect, it was necessary to generate a different finite element mesh for each set of geometric parameters. This was achieved using the Abaqus/CAE Python scripting interface: for each set of model parameters, routines written in Matlab code were used to generate a Python script which was then executed by Abaqus/CAE to produce a model input file (see Figure 18). This was done automatically for both the thermal and mechanical parts of the analysis. The resulting input files were transferred to a server where the models were run using Abaqus/Standard v6.12. Finally, once all models for the whole range of parameters were completed, the resulting data files were transferred back to a desktop machine ready for extraction of the results. Further Matlab code was used to control the processes of model generation, execution and data extraction.

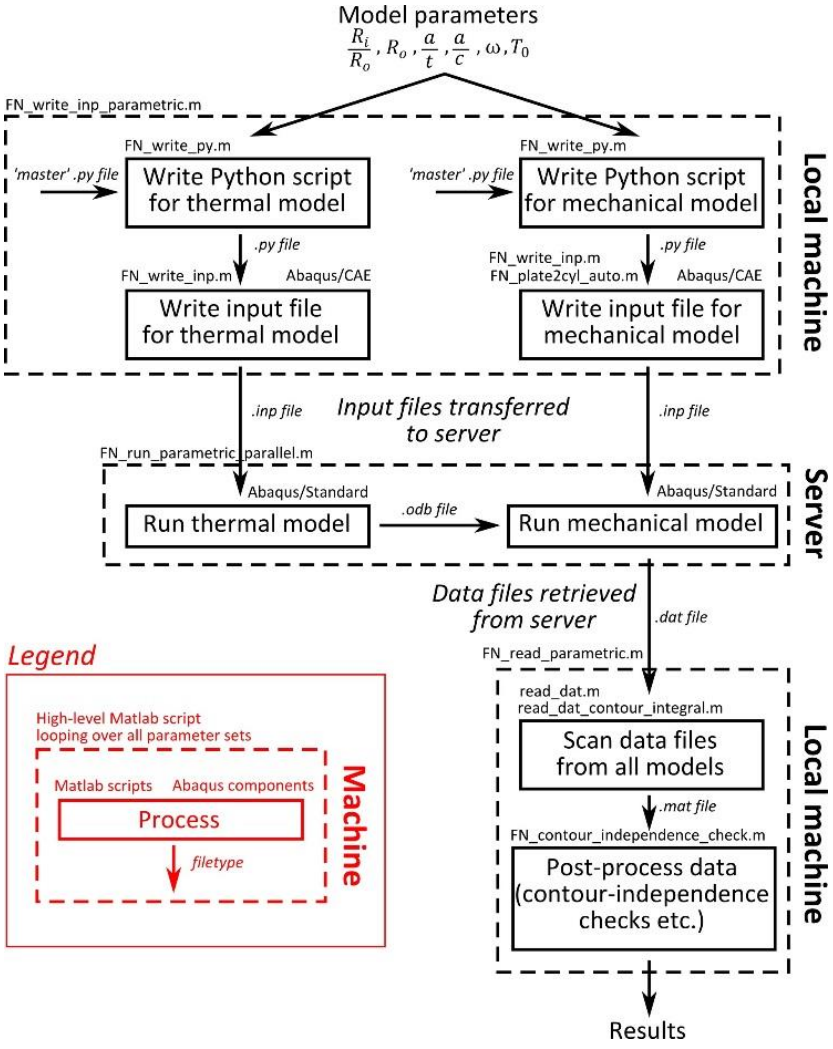

Figure 18: Flowchart detailing how the parametric analysis was performed. The range of model parameters used is given in Table 1.

All of the Abaqus/Standard analyses were performed using a server machine with 12 Intel Xeon x5670 CPUs and 50 GB of memory running CentOS Linux. To make best use of system resources, the Matlab script used to manage model execution (FN_run_parametric_parallel.m) ran several models in parallel. This reduced the effect of Abaqus/Standard's CPU time bottlenecks, in particular model pre-processing, on the total runtime for the parametric series as a whole.

Appendix 4: Thermal modelling boundary conditions

During the NESC-1 test the internal surface of the specimen was quenched using a continuous spray of water at 5 °C supplied from a storage tank. In the thermal models, the heat flux per unit area across the quenched internal surface of the specimen (q) was defined as:

$$q = -h(T - T_s) \tag{5}$$

Where T is the temperature of the specimen (at the inner surface), T_s is a constant sink temperature of 5 °C and h is a film coefficient of the thermal boundary layer. Temperature measurements carried out during the NESC-1 programme suggested a film coefficient h in the range 9 - 15 kW m^{-2} K^{-1} [18]. A sensitivity study was performed to assess the effect of the film coefficient. Figure 19 shows the temperature profiles at three points through the cylinder wall for extreme values of h. The temperature field is fairly insensitive to differences in film coefficient in the range 9 - 15 kW m^{-2} K^{-1}. However, a value of 9 kW m^{-2} K^{-1} produced the temperature field which corresponded most closely to that measured during the NESC-1 programme and so this value was used in all subsequent models.

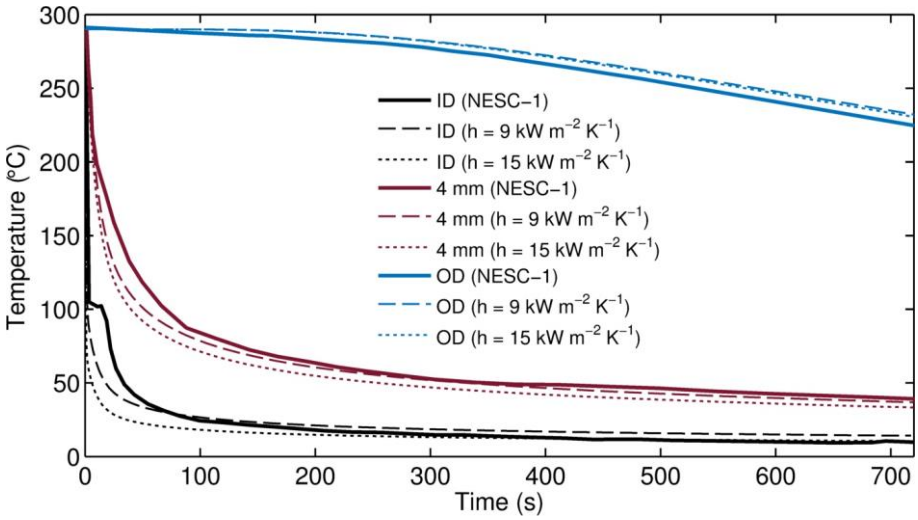

Figure 19: Temperature history of the NESC-1 specimen at the Inner Diameter (ID), 4 mm from the Inner Diameter (4 mm) and the Outer Diameter (OD). The measured temperature history of NESC-1 is shown alongside results from FE models using different heat transfer film coefficients.

The thermal model mesh was split into two layers, one representing the austenitic clad material and one representing the ferritic HAZ and base materials. Mesh sensitivity studies were performed to ensure that the calculated temperature field was insensitive to further refinement of the mesh in the radial direction.

References

[1] IAEA, "Guidelines on Pressurized Thermal Shock Analysis for WWER Nuclear Power Plants," IAEA-EBP-WWER-08(Rev. 1), 2006.

[2] R. Woods, N. Siu, A. Kolaczkowski, and W. Galyean, "Selection of pressurized thermal shock (PTS) transient to include in PTS risk analyses," *International Journal of Pressure Vessels and Piping*, vol. 78, no. 2–3, pp. 179–183, 2001.

[3] IAEA, "Pressurized Thermal Shock in Nuclear Power Plants: Good Practices for Assessment," IAEA, 1627, 2010.

[4] D. P. G. Lidbury, A. H. Sherry, C. E. Pugh, and B. R. Bass, "The performance of large-scale structures and validation of assessment procedures," in *Comprehensive Structural Integrity*, vol. 7, R. A. Ainsworth and K.-H. Schwalbe, Eds. Elsevier, 2003, pp. 529–587.

[5] C. E. Pugh and B. R. Bass, “A Review of Large-Scale Fracture Experiments Relevant to Pressure Vessel Integrity Under Pressurized Thermal Shock Conditions,” U.S. Nuclear Regulatory Commission Office of Nuclear Regulatory Research, NUREG/CR-6699, 2001.
[6] C. E. Pugh, B. R. Bass, and T. L. Dickson, “Role of probabilistic analysis in integrity assessments of reactor pressure vessels exposed to pressurized thermal-shock conditions,” *Engineering Failure Analysis*, vol. 14, no. 3, pp. 501–517, 2007.
[7] L. Hodulak, J. G. Blauel, D. Siegele, and B. Urich, “Thermal shock experiments on cracked cladded plates,” *Nuclear Engineering and Design*, vol. 188, no. 2, pp. 139–147, 1999.
[8] M. Scibetta, J. Schuurmans, and E. Lucon, “Experimental study of the fracture toughness transferability to pressurized thermal shock representative loading conditions,” in *ASTM Special Technical Publication*, 2009, vol. 1508 STP, pp. 499–517.
[9] P. J. Budden and J. K. Sharples, “Treatment of secondary stresses,” in *Comprehensive Structural Integrity, Volume 7*, 1st ed., R. A. Ainsworth and K.-H. Schwalbe, Eds. Elsevier-Pergamon, 2003, pp. 245–288.
[10] *R6: Assessment of the Integrity of Structures Containing Defects, Revision 4, Amendment 11*. EDF Energy, Gloucester, 2015.
[11] R. A. Ainsworth, “The treatment of thermal and residual stresses in fracture assessments,” *Engineering Fracture Mechanics*, vol. 24, no. 1, pp. 65–76, 1986.
[12] P. J. Withers, “Residual stress and its role in failure,” *Reports on Progress in Physics*, vol. 70, no. 12, pp. 2211–2264, 2007.
[13] *BS 7910:2013 - Guide to methods for assessing the acceptability of flaws in metallic structures*. BSi, 2013.
[14] R. A. Ainsworth, “Consideration of elastic follow-up in the treatment of combined primary and secondary stresses in fracture assessments,” *Engineering Fracture Mechanics*, vol. 96, pp. 558–569, 2012.
[15] G. Qian, V. F. Gonzalez-Albuixech, and M. Niffenegger, “In-plane and out-of-plane constraint effects under pressurized thermal shocks,” *International Journal of Solids and Structures*, vol. 51, no. 6, pp. 1311–1321, 2014.
[16] Y. He and T. Isozaki, “Fracture mechanics analysis and evaluation for the RPV of the Chinese Qinshan 300 MW NPP under PTS,” *Nuclear Engineering and Design*, vol. 201, no. 2, pp. 121–137, 2000.
[17] D. Siegele, L. Hodulak, I. Varfolomeyev, and G. Nagel, “Failure assessment of RPV nozzle under loss of coolant accident,” *Nuclear Engineering and Design*, vol. 193, no. 3, pp. 265–272, 1999.
[18] R. Bass, J. Wintle, R. C. Hurst, and N. Taylor, “NESC-I Project Overview,” European Commission, 2001.
[19] R. Rintamaa, K. Wallin, H. Keinänen, T. Planman, and H. Talja, “Consistency of fracture assessment criteria for the NESC-1 thermal shock test,” *International Journal of Pressure Vessels and Piping*, vol. 2–3, pp. 125–135, 2001.
[20] *Abaqus Analysis User’s Manual v6.12*. Dassault Systèmes, 2012.
[21] *Abaqus/CAE v6.12*. Providence, RI, USA: Dassault Systemes Simulia Corp., 2012.
[22] MATLAB®, *version 8.5.0.197613 (R2015a)*. Natick, USA: The Mathworks Inc.
[23] D. P. G. Lidbury, B. R. Bass, S. Bhandari, and A. H. Sherry, “Key features arising from structural analysis of the NESC-1 PTS benchmark experiment,” *International Journal of Pressure Vessels and Piping*, vol. 78, pp. 225–236, 2001.
[24] M. Kuna, *Finite Elements in Fracture Mechanics: Theory - Numerics - Applications*. Springer, 2013.
[25] J. R. Rice, “A path independent integral and the approximate analysis of strain concentration by notches and cracks,” *Journal of Applied Mechanics*, vol. 35, pp. 379–386, 1968.
[26] C. F. Shih, B. Moran, and T. Nakamura, “Energy release rate along a three-dimensional crack front in a thermally stressed body,” *International Journal of Fracture*, vol. 30, no. 2, pp. 79–102, 1986.

[27] W. Brocks, A. Cornec, and I. Scheider, “Computational aspects of nonlinear fracture mechanics,” in *Comprehensive Structural Integrity*, vol. 7, R. de Borst and H. A. Mang, Eds. Elsevier, 2003, pp. 127–209.
[28] R. Hurst, N. Taylor, D. McGarry, B. R. Bass, R. Rintamaa, and J. Wintle, “Evaluating the NESC-I test and the integrated approach to structural integrity assessment,” *International Journal of Pressure Vessels and Piping*, vol. 78, no. 2–3, pp. 213–224, 2001.
[29] C. Betegon and J. W. Hancock, “Two-parameter characterization of elastic-plastic crack-tip fields,” *Journal of Applied Mechanics, Transactions of the ASME*, vol. 58, pp. 104–110, 1991.
[30] M. Gupta, R. C. Alderliesten, and R. Benedictus, “A review of T-stress and its effects in fracture mechanics,” *Engineering Fracture Mechanics*, vol. 134, pp. 218–241, 2015.
[31] M. Chen, F. Lu, R. Wang, P. Huang, X. Liu, G. Zhang, and C. Xu, “The deterministic structural integrity assessment of reactor pressure vessels under pressurized thermal shock loading,” *Nuclear Engineering and Design*, vol. 288, pp. 130–140, 2015.
[32] G. G. Chell, “Incorporation of residual and thermal stresses in elastic-plastic fracure mechanics design,” in *Advances in Elasto-Plastic Fracture Mechanics: Proceedings of a Seminar held at the Joint Research Centre of the Commission of the European Communities*, 1980, pp. 359–384.
[33] G. G. Chell and R. P. Harrison, “Stress intensity factors for cracks in some fracture mechanics test specimens under displacement control,” *Engineering Fracture Mechanics*, vol. 7, no. 2, pp. 193–203, 1975.
[34] G. S. Schajer and P. S. Whitehead, “Chapter 2: Hole Drilling and Ring Coring,” in *Practical Residual Stress Measurement Methods*, G. S. Schajer, Ed. Wiley, 2013, pp. 29–64.
[35] E. J. Hearn, *Mechanics of Materials 2*, 3rd ed. Butterworth Heinemann, 1997.
[36] S. Chapuliot, “K_I formula for pipes with a semi-elliptical longitudinal or circumferential, internal or external surface crack,” CEA Saclay, CEA-R-5900, 2000.